Tip-tilt estimation and correction using FQPM coronagraphic images

M. Mas[1], P. Baudoz[1], G. Rousset[1], and R. Galicher[1,2,3]

[1] LESIA, Observatoire de Paris, CNRS, Univ. Paris Diderot – Paris 7, UPMC Paris 6, 5 place Jules Janssen, 92195 Meudon, France
e-mail: `marion.mas@obspm.fr`
[2] National Research Council Canada, Herzberg Institute of Astrophysics, 5071 West Saanich Road, Victoria, BC, V9E 2E7, Canada
[3] Dept. de Physique, Université de Montréal, C.P. 6128 Succ. Centre-ville, Montréal, Qc, H3C 3J7, Canada

ABSTRACT

Context. Direct imaging of exoplanets located a few AU from their hosting star requires angular resolution at the diffraction limit of large telescopes and a contrast level in the image of 10^5 to 10^{10}. Simultaneous use of adaptive optics and coronagraphy is mandatory to fulfil these requirements.
Aims. Coronagraphs are usually very sensitive to pointing errors upstream of their focal plane mask. Approaches to measuring these errors in conventional adaptive optics systems consist in setting a wavefront sensor in an additional channel. Differential aberrations between the coronagraphic channel and the additional one induce a loss in performance. To tackle this limitation, we propose a new technique for measuring the tip-tilt errors directly from the coronagraphic image.
Methods. Our method uses the relations between the intensity distribution in the coronagraphic image and upstream tip-tilt errors. We also propose a method of estimating the tip-tilt errors downstream of the focal plane mask. We validate at visible wavelength our upstream and downstream tip-tilt estimation and compensation techniques with numerical simulation images and on laboratory images.
Results. Numerical simulations predict that our techniques correct for the tip-tilt errors to a $1.3 \times 10^{-2} \lambda/D$ level when considering a $\lambda/40$ wavefront error upstream of the coronagraph. In laboratory, where the coronagraph is mostly limited by wavefront errors, we correct for the tip-tilt errors with an accuracy better than $6.5 \times 10^{-2} \lambda/D$.
Conclusions. We demonstrate in numerical simulations and in laboratory that our technique can efficiently estimate the tip-tilt errors directly from the coronagraphic image with no additional channel. It is robust and can be used with small wavefront errors. It should be applicable to planet imager systems currently in preparation, such as SPHERE and MIRI/JWST.

Key words. instrumentation: adaptive optics – instrumentation: high angular resolution – methods: laboratory – techniques: image processing

1. Introduction

During the past decade, our knowledge of formation and evolution of planetary systems has been significantly increased. About seven hundred exoplanets have been discovered by different techniques. The diversity of what we observe today is broader than what was expected 20 years ago. Even though a few exoplanets can be characterized by transit spectroscopy, the majority cannot be and are still unknown in terms of temperature and composition. A promising technique to spectroscopically study exoplanets located at a few AU from their hosting stars is direct imaging. It is, however, a challenging goal for two reasons. On one hand, the planet-star angular separation is close to the telescope resolution. On the other hand, the high star-planet flux ratio (from 10^5 to 10^{10}) requires high contrast imaging techniques like coronagraphy. Several coronagraphic instruments are currently developed for ground-based telescopes (SPHERE, GPI, Beuzit et al. 2008; Macintosh et al. 2008) and space applications (MIRI/JWST, Boccaletti et al. 2005).

To maximize the number of exoplanet images, one needs high-performance coronagraphs with small inner working angles (IWA, angular separation at which the planet's useful throughput first reaches half of the peak throughput, Guyon et al. 2006). Coronagraphs with small IWA are very sensitive to low-order aberrations and small pointing errors upstream of their focal plane mask. These aberrations diffract a part of the stellar light through the coronagraph aperture and strongly decrease the coronagraph performance (Lloyd & Sivaramakrishnan 2005; Sivaramakrishnan et al. 2005; Shaklan & Green 2005). To detect very faint companions close to their stars, it is then necessary to accurately measure and correct for the low-order aberrations such as tip-tilt, focus, and astigmatism. Classical adaptive optics solution implies spatially splitting the coronagraphic beam to create a wavefront sensing channel and a scientific channel. This split induces differential aberrations between the two channels and may prevent accurate wavefront estimations. Techniques optimized for coronagraphic images have been proposed (Guyon et al. 2009; Sivaramakrishnan et al. 2008) that rely on a wavefront sensing channel using dedicated optical setup that needs to be calibrated.

In this paper, we focus on the tip-tilt errors that are the most limiting aberrations for a coronagraph. We propose to measure these errors directly in the coronographic image with no additional channel. Our technique estimates both tip-tilt errors upstream and downstream of the coronagraphic focal plane mask. The upstream errors push the beam out of the focal plane mask and directly degrade the coronagraphic efficiency. The downstream errors only induce shifts of the whole image on the
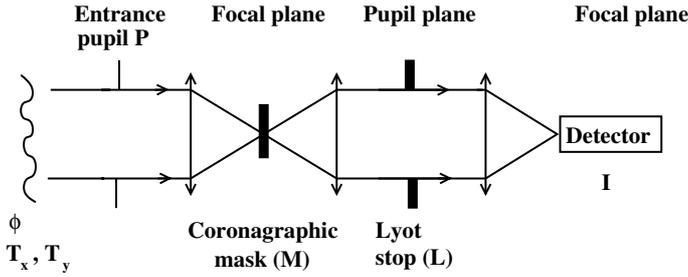
Entrance pupil P **Focal plane** **Pupil plane** **Focal plane**

Fig. 1. Principle of the considered coronagraphic instrument.

Fig. 2. *Left*: central area S of the coronagraphic image I_c for a tip-tilt errors upstream of the coronagraph: $T_x = 0.2\lambda/D$, $T_y = 0$ and no WFE $\phi = 0$. *Right*: coordinate axes.

detector but we need to estimate them to control the upstream errors. We evaluate the performance of our technique on both numerical simulations and laboratory tests for the four quadrant phase mask coronagraph (FQPM, Rouan et al. 2000).

In Sect. 2, we present the FQPM image distortions induced by tip-tilt errors. We then derive formalism to estimate the tip-tilt upstream of an FQPM directly from the coronagraphic images. In Sect. 3, we use numerical simulations to determine the performance of the upstream tip-tilt error estimation and correction, ignoring the downstream error impact. In Sect. 4, we explain how to estimate for tip-tilt errors downstream of the coronagraph from the coronagraphic images and we give the technique performance, ignoring upstream errors. We finally present laboratory performance of the combined upstream and downstream tip-tilt techniques in Sect. 5. We discuss in Sect. 6 some practical issues that affect the performance of our techniques.

2. Estimation of tip-tilt errors upstream of the coronagraph

The variables used in this paper are recalled in Appendix A.

2.1. Numerical model of the instrument

We consider an instrument having a full disk pupil and equipped with a coronagraph that rejects the stellar light as a means to do exoplanet direct imaging. The instrument principle is shown in Fig. 1. In the entrance pupil P, the aberrations upstream of the coronagraphic mask are characterized by the wavefront error (WFE) ϕ linked to the optical train quality. In addition, we consider the tip and tilt modes linked to pointing errors, denoted T_x and T_y expressed in λ/D normalized angles, where λ is the wavelength and D the telescope diameter. The coronagraphic mask M is installed in the first focal plane where the telescope point spread function (PSF) is formed. The light diffracted by the coronagraph is filtered by the Lyot stop L placed in the relayed pupil image plane. Because of upstream wavefront aberrations, a part of the stellar light goes through the coronagraph and creates the speckle pattern in the second focal plane of the instrument, where the detector is placed.

We use Fourier optics and Fraunhofer diffraction in our model. The monochromatic electric field ψ' upstream of the coronagraph in the entrance pupil P is

$$\psi'(\xi, \nu) = P(\xi, \nu)e^{\left(i\pi\left(2\phi(\xi,\nu)/\lambda + (\xi T_x + \nu T_y)\right)\right)}, \quad (1)$$

where (ξ, ν) are the spatial coordinates in the entrance pupil plane normalized by $D/2$ and M is the FQPM (Rouan et al. 2000) that induces a π phase shift on two focal plane quadrants in a diagonal and 0 on the two other quadrants. The Lyot stop is
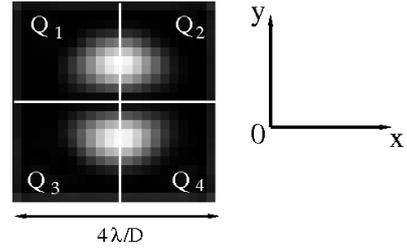
put in the relayed pupil plane and the resulting electric field ψ can be written as

$$\psi = \mathcal{F}^{-1}\left(\mathcal{F}(\psi')M\right)L, \quad (2)$$

where $\mathcal{F}$ is the Fourier transform operator and $\mathcal{F}^{-1}$ its inverse. Finally, the intensity of the coronagraphic image I_c recorded by the detector is

$$\begin{aligned}I_c &= |\mathcal{F}(\psi)|^2 \\ &= \left|\mathcal{F}\left[\mathcal{F}^{-1}\left(\mathcal{F}\left(Pe^{\left(i\pi\left(2\phi(\xi,\nu)/\lambda + (\xi T_x + \nu T_y)\right)\right)}\right)M\right)L\right]\right|^2. \quad (3)\end{aligned}$$

From Eq. (3), we can compute how the tip-tilt errors T_x and T_y affect the intensity distribution I_c. The larger T_x and T_y are, the more the telescope PSF is badly centred on M and the brighter the intensity is after the coronagraph. Even for tip-tilt errors of the order of a few tenths of the telescope diffraction limit λ/D, the star light leaks dramatically increase and may dominate the speckles related to a WFE ϕ (Lloyd & Sivaramakrishnan 2005). If there is no WFE or tip-tilt errors upstream of the coronagraph ($\phi = 0$ and $T_x = T_y = 0$), then $I_c = 0$ (Rouan et al. 2002; Abe et al. 2003; Lloyd et al. 2003). If there are tip-tilt errors, they induce two main bright speckles close to the centre of the FQPM coronagraphic image. Figure 2 shows the central area of the resulting coronagraphic image I_c. It is not obvious that we can retrieve the tip-tilt errors from such an image since speckles split along y-axis, whereas tip-tilt errors is along x-axis. The two bright speckles are mostly symmetrical, but we will see that a slight asymmetry can be detected.

Because tip-tilt errors increase the light intensity and modify its distribution in the central area of I_c, we propose to compute intensity differences as done with a four quadrant detector for tracking system (Tyler & Fried 1982). We select on I_c a squared central area S with a size of a few λ/D. We divide S in four equal quadrants Q_i (Fig. 2) on which we compute a normalized integrated intensity I_i

$$I_i = \frac{\int_{Q_i} I_c \mathrm{d}s}{\int_S I_{nc} \mathrm{d}s}. \quad (4)$$

The normalizing factor is a precalibrated, integrated intensity on the area S for a non-coronagraphic image I_{nc}, computed with Eq. (3) where M is constant and equal to 1, $T_x = 0$ and $T_y = 0$, but keeping the Lyot stop L and the WFE ϕ.

We then define the intensity differences ΔI_x and ΔI_y in the central area S, which will allow us to estimate the tip-tilt errors:

$$\Delta I_x = (I_2 + I_4) - (I_1 + I_3), \quad (5)$$
$$\Delta I_y = (I_1 + I_2) - (I_3 + I_4). \quad (6)$$

Table 1. Numerical simulation conditions with f the spatial frequency.

λ	800 nm
Initial WFE (ϕ)	0 or 20 nm rms
ϕ Power spectral density	f^{-2}, random draw
Pupil	Unobscurated disk
Pupil sampling	128×128 pixels
Lyot stop size	100%
Coronagraph	Perfect FQPM
Pixel size	$\lambda/4D$
Image size	$128\lambda/D \times 128\lambda/D$
Quadrant size (Q_i)	$2\,\lambda/D \times 2\lambda/D$

The challenge is to estimate T_x and T_y from the scientific image (using ΔI_x and ΔI_y) with no additional wavefront sensor channel. If no coronagraph is used, the link between T_x and ΔI_x (or T_y and ΔI_y) is straightforward (Tyler & Fried 1982). We show in the next section that ΔI_x and ΔI_y both depend on T_x and T_y. To quantify the impact of tip-tilt errors on the star rejection efficiency of the coronagraph, we first define the performance metric as the coronagraphic peak attenuation A

$$A = \frac{\max(I_{\mathrm{nc}})}{\max(I_{\mathrm{c}})}, \tag{7}$$

where the maxima of the two images are computed in the central area S. In the case of small pure tip-tilt errors (T_x and T_y, $<0.5\ \lambda/D$), we found from numerical simulation that, for the FQPM coronagraph, A can be written as

$$A \simeq \frac{1}{0.56(T_x^2 + T_y^2)}. \tag{8}$$

2.2. Numerical simulation of the tip-tilt error effects

In this section, we explain how to estimate the tip-tilt errors, T_x and T_y, from the intensity differences ΔI_x and ΔI_y. The numerical simulation conditions are summarized in Table 1.

To simulate the FQPM coronagraph, we generate a four quadrant mask M of 512×512 pixels (size of the images), centred between the four central pixels. The phase is π on two quadrants and 0 on the two others. We then form an image centred on the mask. To avoid pupil boundary sampling errors, we have to use a specific entrance pupil P. This pupil is computed to give the perfect rejection through FQPM propagation for no aberrations with a Lyot stop of 100%.

2.2.1. Simulation with no wavefront error ($\phi = 0$)

We first show the evolution of the attenuation A and of the intensity differences ΔI_x and ΔI_y versus tip-tilt errors for a few particular cases summarized in Table 2. We introduce a number of tip-tilt errors values, $T_x = [0, 0.05, 0.1, 0.4]\ (\lambda/D)$ and $T_y = 0$ upstream of the coronagraph and we consider no WFE: $\phi = 0$. The coefficient β is a multiplicative coefficient determined by numerical simulations (see Appendix B). It depends on the pixel sampling. As expected, the performance of the coronagraph degrades, while the tip-tilt grows because the star image is not centred on the focal plane mask M. The larger the tip-tilt errors, the lower the attenuation and the larger the intensity difference ΔI_x. In the case of no tip-tilt errors, the intensity differences ΔI_x and ΔI_y are nought and the attenuation A is infinite. With $\phi = 0$ and $T_y = 0$, the intensity difference ΔI_y is nought whatever the T_x

Table 2. Numerical simulated values for attenuation A, intensity differences ΔI_x and ΔI_y for $T_x = [0, 0.05, 0.1, 0.4]\lambda/D$, and $T_y = 0$. $\phi = 0$.

$\phi = 0, T_y = 0$				
Additional x-tilt $T_x\ (\lambda/D)$	Attenuation A	$\frac{\Delta I_x}{\beta}$	$\frac{\Delta I_y}{\beta}$	T_x^3
0.0	Infinite	0	0	0
0.05	722	1.5e-4	0	1.2e-4
0.10	181	1.2e-3	0	1.0e-3
0.40	14	6.4e-2	0	6.4e-2

Table 3. Numerical simulated values for attenuation A, intensity differences ΔI_x and ΔI_y, and Eqs. (9), and (10). $T_x = [0, 0.05, 0.1, 0.4]$, $T_y = 0.05\lambda/D$. $\phi = 0$.

$\phi = 0, T_y = 0.05\ \lambda/D$					
T_x	A	$\frac{\Delta I_x}{\beta}$	$\frac{\Delta I_y}{\beta}$	$T_x^3 + 4T_xT_y^2$	$T_y^3 + 4T_yT_x^2$
0.0	722	0	1.5e-4	0	1.2e-4
0.05	327	7.6e-4	7.6e-4	6.2e-4	6.2e-4
0.10	121	2.4e-3	2.6e-3	2.0e-3	2.1e-3
0.40	12	6.8e-2	3.3e-2	6.8e-2	3.2e-2

value. We found that ΔI_x and T_x are closely linked by the relation $\frac{\Delta I_x}{\beta} \sim T_x^3$ (Table 2). We can also note that the variation of the attenuation A is inversely proportional to the square of T_x as given by Eq. (8).

When introducing an additional error $T_y = 0.05\ (\lambda/D)$ on the y axis, we observed a coupling of the two axes in the computed intensity differences (Table 3). In particular, $\frac{\Delta I_y}{\beta}$ is not constant but increases with T_x. Even if T_y is relatively small, $\frac{\Delta I_y}{\beta}$ reaches values close to the values obtained for $\frac{\Delta I_x}{\beta}$. Also, small T_x, the values of $\frac{\Delta I_x}{\beta}$ are affected when compared to the ones presented in Table 2.

Both ΔI_x and ΔI_y depend T_x and T_y. We performed numerical simulations assuming different conditions and $\phi = 0$. We thus determined the relations between ΔI_x, ΔI_y, T_x and T_y for small tip-tilt errors, $<0.5\ (\lambda/D)$, for the two first order terms (see Appendix B)

$$\frac{\Delta I_x}{\beta} = T_x^3 + \alpha T_x T_y^2, \tag{9}$$

$$\frac{\Delta I_y}{\beta} = T_y^3 + \alpha T_y T_x^2. \tag{10}$$

In the specific case of an FQPM coronagraph, $\alpha = 4$. We report in Table 3, the values of $T_x^3 + 4T_xT_y^2$ and $T_y^3 + 4T_yT_x^2$. These values are very close to the intensity differences $\Delta I_x/\beta$ and $\Delta I_y/\beta$, respectively.

2.2.2. Simulation with wavefront error ($\phi \neq 0$)

We now consider a more realistic case with one particular 20 nm rms WFE. In the computed random WFE, there is a small tip-tilt contribution. To study the impact of known tip-tilt errors T_x and T_y, we subtract its own tip-tilt terms to ϕ. The WFE without tip-tilt for this particular draw is 18.6 nm rms. Then we add an x-tilt $T_x = [0, 0.05, 0.1, 0.4]\ (\lambda/D)$ to compute the field ψ' in Eq. (1). The results are presented in Fig. 3 and in Table 4.

We show in Fig. 3 the evolution of the speckles in the coronagraphic image: the images from the left to the right are for a x-tilt $T_x = [0, 0.05, 0.1, 0.4]\ (\lambda/D)$, respectively, and a y-tilt $T_y = 0$.
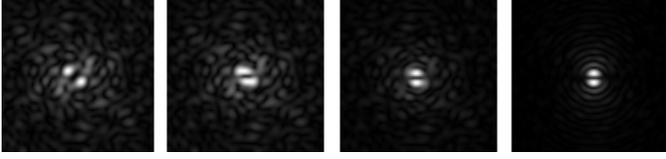
Fig. 3. Coronagraphic images for ϕ rms = 18.6 nm, $T_y = 0$ and different values for T_x, upstream of an FQPM coronagraph. *Left*: reference I_{cr} for $T_x = 0$. Other images I_c for increasing values of T_x from *left to right*: 0.05, 0.1 and 0.4 λ/D. All images normalized to their maximum. Same simulations as in Table 4.

Table 4. Attenuation A and intensity differences ΔI_x, ΔI_y, Δ_x, and Δ_y for $T_x = [0, 0.05, 0.1, 0.4]\lambda/D$, and $T_y = 0$. ϕ rms (tip-tilt subtracted) = 18.6 nm.

		ϕ rms = 18.6 nm, $T_y = 0$			
T_x	A	$\frac{\Delta I_x}{\beta}$	$\frac{\Delta I_y}{\beta}$	Δ_x	Δ_y
0	573	–6.0e-5	1.0e-5	0	0
0.05	500	4.0e-5	–3.3e-4	1.1e-4	–3.5e-4
0.1	165	1.0e-3	–8.7e-4	1.1e-3	–8.8e-4
0.4	13	6.3e-2	–6.2e-3	6.3e-2	–6.2e-3

For the low values of T_x, we observe the deformation of the central speckles, while for the largest tilt, the star leak induced by tilt error dominates and leads to two bright speckles close to the centre.

In Table 4, the obtained attenuation A values are lower than the ones for $\phi = 0$ due to the speckle pattern produced in the image. The sensitivity of ΔI_x to T_x is relatively similar to the previous case ($\phi = 0$). We can however, highlight two differences. The measured intensity difference ΔI_y is never nought and for $T_x = 0$ and $T_y = 0$, ΔI_x and ΔI_y are not nought. The WFE ϕ induces a slight asymmetrical speckle pattern in the focal plane (Perrin et al. 2003), hence in the signals of the selected quadrants. There is thus a new coupling between the x and y axes linked to the WFE-induced speckle pattern. If the coupling is significant, it remains lower for this example than the one obtained with $T_y \neq 0$ as in Table 3. From the values given in the different tables and the images in Fig. 3, we deduce that the impact of a WFE (around 20 nm) will dominate the computation of ΔI_x and ΔI_y for the small tip-tilt errors while it is no longer the case for larger tip-tilt errors ($>0.1\lambda/D$) because of the induced very bright twin speckles.

2.3. Tip-tilt estimators

In practical cases, ϕ is not nought, and we have to deal with WFE induced speckle pattern in the coronagraphic image. Our desire is to measure the tip-tilt errors is to maintain the alignment as close as possible to the one corresponding to a reference image. We call "reference image" (Fig. 3, left) the coronagraphic image corresponding to the smallest tip-tilt error. Its intensity is denoted I_{cr}. To be able to measure any small tip-tilt errors in the current coronagraphic image I_c using the analytical relations given by Eqs. (9) and (10), we subtract the one corresponding to I_{cr} to the intensity differences. We first compute $\Delta I_{x,r}$ and $\Delta I_{y,r}$ from Eq. (6) for I_{cr}. Then, we define two new differences Δ_x and Δ_y, which are linked to T_x and T_y in I_c by

$$\Delta_x = \frac{\Delta I_x - \Delta I_{x,r}}{\beta} \simeq T_x^3 + 4T_x T_y^2, \tag{11}$$

$$\Delta_y = \frac{\Delta I_y - \Delta I_{y,r}}{\beta} \simeq T_y^3 + 4T_y T_x^2. \tag{12}$$

Table 5. Spatial root mean square of ϕ averaged on 100 draws with tip-tilt for I_{cr} computation and without tip-tilt for I_c computation.

	ϕ (nm rms)				
I_{cr}	with tip-tilt	0	5	10	20	40
I_{cs}	w/o tip-tilt	0	4.7	9.5	19	38

In Table 4, we present the values of Δ_x and Δ_y for the considered case, where I_{cr} is the computed image with $T_x = 0$ and $T_y = 0$ (left image in Fig. 3). We observe that Δ_x (with ϕ rms = 18.6 nm) is close to $\frac{\Delta I_x}{\beta}$ when $\phi = 0$ nm rms (Table 2). However, Δ_y is not nought because of asymmetrical speckle pattern in the y direction due to the high-orders of ϕ. Using an iterative process, we demonstrate in the next section that we can estimate T_x and T_y from Eqs. (11) and (12) even with the effects of WFE. To identify the convergence, we propose to compute the attenuation A (Eq. (7)) for each new image obtained after tip-tilt correction. The goal is therefore to maximize A.

To estimate the tip-tilt errors from the measurements, we first have to inverse Eqs. (11) and (12). From these equations, we can write

$$R^3 - 4R^2 \frac{\Delta_x}{\Delta_y} + 4R - \frac{\Delta_x}{\Delta_y} = 0, \tag{13}$$

with

$$R = \frac{T_x}{T_y}. \tag{14}$$

This equation has a unique, real solution R except in the case when the value of $\frac{\Delta_x}{\Delta_y}$ is close to 1. In this case, we make the approximation $R = 1$ (see Appendix B). We derive the general expressions of the estimators $T_{x,\text{est}}$ and $T_{y,\text{est}}$

$$T_{x,\text{est}} = \left(R^2 \frac{\Delta_x}{R^2 + 4} \right)^{1/3}, \tag{15}$$

$$T_{y,\text{est}} = \left(\frac{\Delta_y}{1 + 4R^2} \right)^{1/3}. \tag{16}$$

These estimators depend on the value of R. The ratio $\frac{T_y}{T_x}$ can also be considered. The different cases are developed in the Appendix B. With this method, we are able to estimate the tip-tilt upstream of the coronagraph directly from the coronagraphic image measuring the intensity differences Δ_x and Δ_y.

3. Performance from numerical simulations

In this section, we present the results of tip-tilt estimation and correction by numerical simulations. Parameters of the simulations are given in Table 1 in Sect. 2.2. In the simulations, we drew a set of random WFE ϕ. These WFE are defined by their rms values given in Table 5 for the two cases tip-tilt modes included and subtracted. For each initial WFE including tip-tilt modes, we computed the reference image I_{cr} having no additional tip-tilt ($T_x = 0$ and $T_y = 0$).

To simulate the estimation process, we removed the tip-tilt modes contribution of the initial random WFE and introduced a random additional tip-tilt in T_x and T_y, uniformly drawn between -0.4 and 0.4 λ/D, in order to compute the coronagraphic image I_c by Eq. (3). This couple (T_x, T_y) is different for each random WFE.

For each WFE draw, we determined the estimations $T_{x,\text{est}}$ and $T_{y,\text{est}}$ of the tip-tilt errors T_x and T_y. Estimators $T_{x,\text{est}}$ and $T_{y,\text{est}}$ (Eqs. (15) and (16)) were derived from the intensity differences Δ_x and Δ_y and the ratio $R = \frac{T_x}{T_y}$ with some approximations due to the impact of the WFE ϕ. Once estimated, we compensated for the tip-tilt errors upstream of the coronagraph driving a tip-tilt mirror. In the numerical simulations, we subtract $T_{x,\text{est}}$ and $T_{y,\text{est}}$ from T_x and T_y respectively in Eq. (1). As the estimation is not perfect, we used an iterative process. We recorded the new coronagraphic image I_c, estimated the new residual tip-tilt errors, corrected for them, and repeated the process using a gain equal to 1. The correction loop converges to low values of Δ_x and Δ_y within 15 iterations. The first iteration corresponds to the first correction of the tip-tilt errors, hence to the first value of the residual tip-tilt errors $T_x - T_{x,\text{est}}$ and $T_y - T_{y,\text{est}}$. We first checked that, with no WFE ($\phi = 0$), the tip-tilt correction converges within eight iterations to a residual error of the order of $10^{-8}\lambda/D$.

To study the convergence of the tip-tilt errors estimation under realistic conditions, we present the attenuation A, the absolute tip-tilt errors $((T_x-T_{x,\text{est}})^2+(T_y-T_{y,\text{est}})^2)^{1/2}$ and the absolute intensity difference $((\Delta_x)^2+(\Delta_y)^2)^{1/2}$ with respect to the iteration number for ϕ rms = 19 nm in Fig. 4. In this figure, we present performance for three tip-tilt errors couples (T_x, T_y). For each couple, the WFE draw is different. The three cases we considered behave the same way. There is an oscillation around the best estimation of the tip-tilt errors after a few iterations (Fig. 4, middle), and this tip-tilt error is never as small as in the $\phi = 0$ case. Higher orders in the WFE therefore introduce errors that are not estimated by our approach. We expected this behaviour because $T_{x,\text{est}}$ and $T_{y,\text{est}}$ are derived by assuming that the effect of ϕ is negligeable compared to T_x and T_y. After a few iterations, that assumption is not true anymore and the estimators do not give a sufficiently accurate estimation of the residual tip-tilt errors. For practical applications, we verified that using a loop gain lower than one allows us to reduce the oscillations. To find the iteration corresponding to the smallest tip-tilt errors, we considered the maximum of the attenuation A (Eq. (7)) as a criterium. The attenuation is presented in Fig. 4, top, computed for the same three couples (T_x, T_y). When the attenuation A is maximum, the absolute tip-tilt errors $((T_x - T_{x,\text{est}})^2 + (T_y - T_{y,\text{est}})^2)^{1/2}$ are minimum (Fig. 4). We also present the absolute intensity differences $((\Delta_x)^2+(\Delta_y)^2)^{1/2}$ in the bottom of Fig. 4. The intensity difference decreases significantly down to a level of the order of 10^{-4}. But we were not able to find the minimum of the tip-tilt errors with this parameter, because of the impact of the WFE limiting the validity of our crude model for the estimation.

To determine the accuracy of our upstream tip-tilt errors estimation, we considered a set of hundred random WFE in Table 5. For each random WFE, we estimated the tip-tilt errors and find the iteration corresponding to the best estimation based on our attenuation criterium.

We present the residual y-tilt ($T_y - T_{y,\text{est}}$) in Fig. 5 with respect to the residual x-tip ($T_x - T_{x,\text{est}}$) in λ/D for the best iteration, when the attenuation A is at its maximum. We observe that the accuracy achievable with our method is directly linked to the WFE in the pupil. The higher the WFE, the higher the tip-tilt residual errors too. In Fig. 6, we also show the maximum of the attenuation obtained in the tip-tilt compensation process. For each random WFE (19 nm rms), we plot the attenuation in the coronagraphic image I_c for the best correction of the tip-tilt errors with respect to the attenuation in the initial reference image I_{cr}. Using our method to estimate and compensate for the tip-tilt,
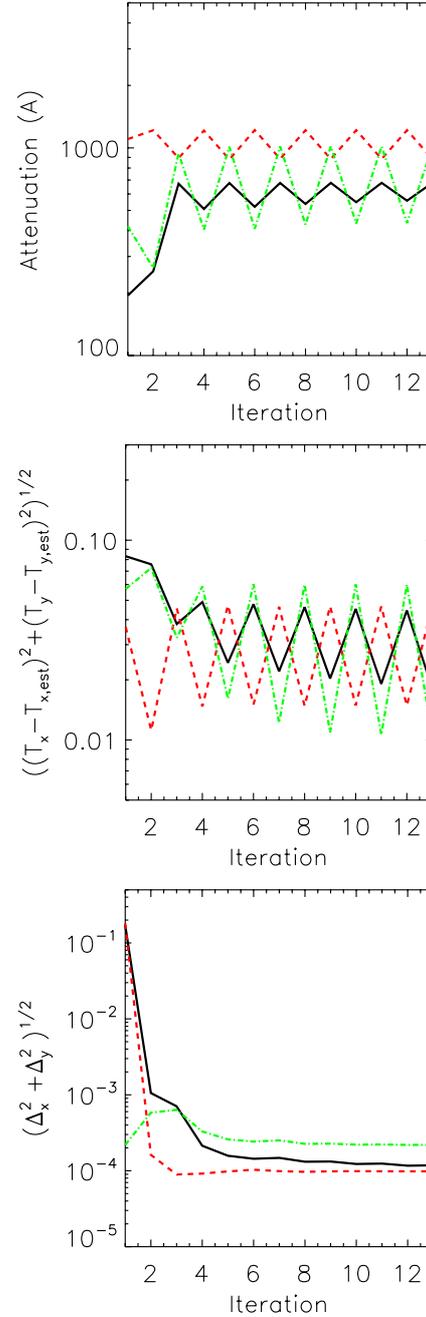

Fig. 4. Simulation results for the different indicators of the convergence: the attenuation A (*top*), the value $((T_x - T_{x,\text{est}})^2 + (T_x - T_{x,\text{est}})^2)^{1/2}$ (*middle*), the value $((\Delta_x)^2 + (\Delta_y)^2)^{1/2}$ (*bottom*) versus the iteration number. $T_{x1} = -0.29\lambda/D$, $T_{y1} = 0.4\lambda/D$ (black full line), $T_{x2} = 0.32\lambda/D$, $T_{y2} = 0.37\lambda/D$ (red dashed line), $T_{x3} = 0.03\lambda/D$, $T_{y3} = -0.05\lambda/D$ (green dotted-dashed line), ϕ rms = 19 nm.

we were able to reach an attenuation higher than the one of the reference image after a few iterations. As a result, the residual tip-tilt errors are smaller after a few iterations than initially.

We report the rms residual values in λ/D for $\phi = [0, 4.7, 9.5, 19, 38]$ nm rms in Table 6. We can estimate the tip-tilt errors with an accuracy of the order of $1.3 \times 10^{-2}\lambda/D$ in the case of a 19 nm rms WFE ($\lambda/40$) and $2.5 \times 10^{-2}\lambda/D$ for 38 nm rms ($\lambda/20$). The residual tip-tilt errors are roughly proportional to the rms WFE, as expected from the analytical derivation of extreme adaptive optics PSF (Perrin et al. 2003). With our method, we are able to estimate and compensate for tip-tilt
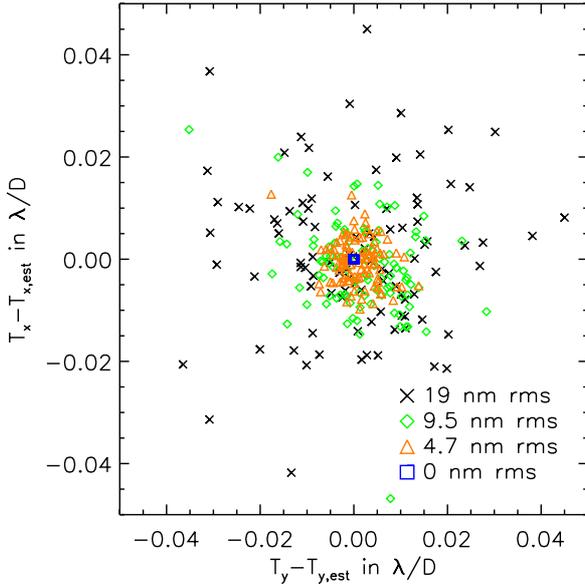
Fig. 5. Optimized residual tip-tilt errors. 100 random WFE of 19 nm rms (black crosses), 9.5 nm rms (green diamonds), 4.7 nm rms (orange triangles), and 0 nm rms (blue square). For each random WFE, we add a tip-tilt T_x and T_y between -0.4 and 0.4 λ/D.
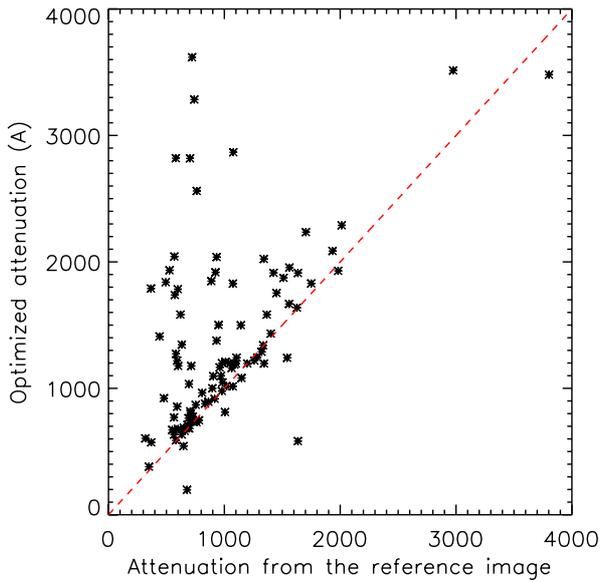

Fig. 6. Optimized attenuation $A = \frac{\max(I_{nc})}{\max(I_c)}$ obtained from a coronagraphic image I_c after tip-tilt compensation vs. attenuation $A = \frac{\max(I_{nc})}{\max(I_{cr})}$ obtained from the reference image I_{cr}. 100 random WFE of 19 nm rms.

errors upstream of a coronagraphic mask by directly computing the intensity differences on the final coronagraphic image. We demonstrate from numerical simulations that we can stabilize a beam on an FQPM coronagraph with a very good pointing accuracy.

4. Estimation of the tip-tilt errors downstream of the coronagraph

The measurement of the tip-tilt described in Sect. 2 assumes that there are no tip-tilt errors introduced downstream of the coronagraph, i.e. that the coronagraph axis is always centred on the same position on the detector. If this axis position drifts, the

Table 6. Rms residual tip-tilt errors values in λ/D after attenuation maximization.

ϕ (nm rms)	0	4.7	9.5	19	38
Tip-tilt (λ/D rms)	8.0e-9	3.2e-3	7.3e-3	1.3e-2	2.5e-2

detector records a shifted image. If this misregistration occurs between the recording of the reference image I_{cr} and any other image I_c of the correction loop, the intensity variations Δ_x and Δ_y are biased ($\Delta_x \neq 0$ and $\Delta_y \neq 0$ for $T_x = T_y = 0$). As the estimators $T_{x,\text{est}}$ and $T_{y,\text{est}}$ of the tip-tilt are linked to Δ_x and Δ_y (Eqs. (15) and (16)), our estimation of the tip-tilt errors upstream of the focal plane mask is incorrect. We then need to estimate these tip-tilt errors downstream of the focal plane mask to accurately estimate the tip-tilt errors upstream of the focal plane mask.

Solutions have already been proposed for precisely measuring the astrometry of the sources in coronagraphic images (Sivaramakrishnan et al. 2006; Marois et al. 2006) and implemented (Zimmerman et al. 2010). They rely on a periodic structure added in the pupil plane upstream of the coronagraph to create fiducial images of the star with known positions. These solutions require a change in phase or amplitude upstream of the coronagraph that is not always simple to implement. We propose a solution that does not change the beam upstream of the coronagraph.

We denote I_{cs} as the intensity of the shifted coronagraphic image. We choose to measure the shift of I_{cs} with respect to the reference image I_{cr} (defined in Sect. 2.3). We consider that there is no tip-tilt error upstream of the coronagraph ($T_x = T_y = 0$) and a stable WFE. The image I_{cs} is then the same than I_{cr} but shifted in the final focal plane of γ_x and γ_y (in λ/D) in the x and y directions, respectively. Both γ_x and γ_y describe the shift of the detector compared to the coronagraph axis. To estimate γ_x and γ_y, we propose to compute the image correlation C between I_{cs} and I_{cr} and estimate in C the position of the correlation peak.

As shown in Fig. 3, the maximum intensity of the coronagraphic image can be quickly predominated by tip-tilt errors upstream of the coronagraph. This would bias the estimation of the detector position. As shown in the same figure, low values of upstream tip-tilt mainly affects the image within a few λ/D around the coronagraph axis. The intensity distribution at distances of tens of λ/D is a speckle pattern produced by high spatial frequency defects of the optical elements upstream of the coronagraph, and they are less sensitive to tip-tilt. We can take advantage of these speckles to measure the global image shift.

To compute the image correlation, we consider the speckles located further away than 10 λ/D of the coronagraph axis (Fig. 7, top). In the simulation presented in this section, we could have kept all the speckles further away than 10 λ/D because no detection noise was added to the speckles. In the realistic case, since the mean intensity of the speckles decreases with axis distance, the signal-to-noise ratio (SNR) for the speckles drops radially because of the detector readout noise and the speckle photon noise. Thus, to optimize the SNR in the image correlation, we need to define an outer limit of the area used for the correlation for each detection environment (readout noise, incoming flux). We choose arbitrarily to simulate an outer limit of 40 λ/D diameter to consider the effect of this truncating on the estimation of γ_x and γ_y. Indeed, the autocorrelation of this ring-shape mask Γ changes the shape of the image correlation. However, its structure is a smooth halo of width of a few tens of λ/D, while the

Fig. 8. Residual shift of the image I_{cs} measured in λ/D as a function of the iteration number. Black full curves (green dashed curves) stands for shift in x (y) directions. ϕ rms = 20 nm, 20 random draws of the WFE. $\gamma_x = 1.2\ \lambda/D$, $\gamma_y = 0.6\ \lambda/D$.
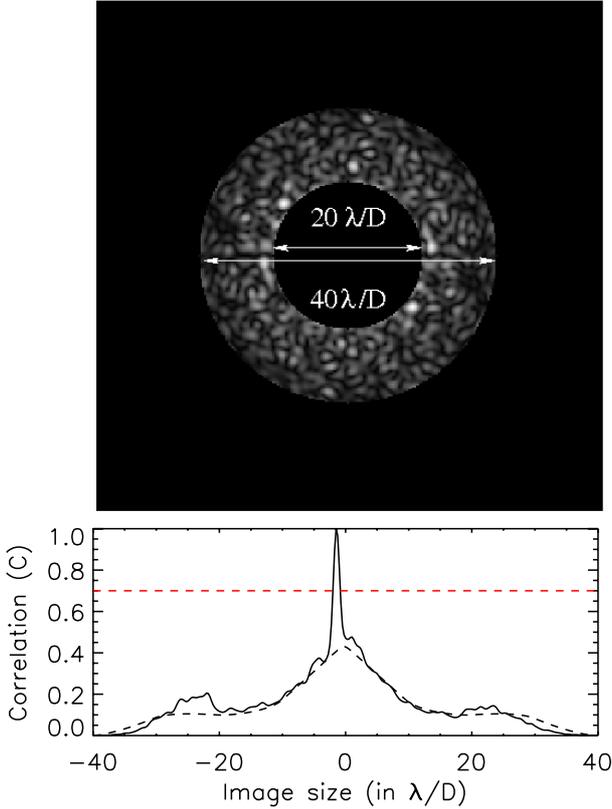
Fig. 7. *Top*: bright ring with speckles considered to estimate the detector shift. *Bottom*: x cut of the correlation. Shift of 1.2 λ/D in the x direction and 0.6 λ/D in the y direction. Dashed black curve: correlation of ring shape mask M. Dashed straight red line: treshold level.

correlation of the speckles creates a thin peak of $2\lambda/D$ width (Fig. 7, bottom). To avoid the bias introduced by the autocorrelation, we select the main peak of the image correlation by applying a threshold. We use a 70% threshold in our numerical simulations. We then compute the centre of gravity of the thresholded image C to get an estimation of the 2D shift of the detector.

We assess the accuracy of the estimation considering the same assumptions as in Sect. 2.2. The inner and outer rings of Γ are defined in Fig. 7 (top). First, we defined the reference image I_{cr} created with a random WFE of 20 nm rms. Then we numerically shift this image with $\gamma_x = 1.2\ \lambda/D$ and $\gamma_y = 0.6\ \lambda/D$ to create I_{cs}. We compute the correlation C and measure the position of the correlation peak by calculating the centre of gravity on thresholded C. The first estimate of the movement ($\gamma_{x,\,est}$ and $\gamma_{y,\,est}$) is not perfect so we need to iterate to improve this measurement. To do so, we numerically shift the previous image by $(-\gamma_{x,\,est}, -\gamma_{y,\,est})$ and compute the new correlation C for this new image and iterate the procedure a few times.

We repeat this simulation for 20 different random WFE of 20 nm rms. We report the error between the estimated position and the real position as a function of the iteration in Fig. 8. The first iteration corresponds to the first correction of the image shift, hence to the first value of the residual shift errors $\gamma_x - \gamma_{x,\,est}$ and $\gamma_y - \gamma_{y,\,est}$. The different curves stand for various WFE draws. After the first correction (iteration 1), the error of the estimation is below $0.06\lambda/D$, which corresponds to an error of ~0.25 pixels. After the third iteration, we are able to shift the image I_{cs} with an accuracy of 0.01 λ/D (0.04 pixels).

In a realistic case, tip-tilt errors upstream and downstream of the coronagraph can occur at the same time. To keep the source
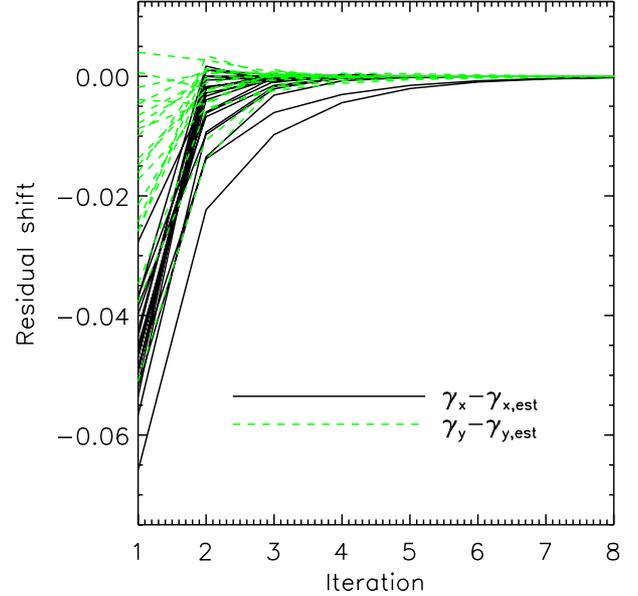
well centred on the coronagraph, the method described in Sect. 2 can only be applied if the tip-tilt error downstream of the coronagraph is corrected for. We propose then to apply the tip-tilt correction in three successive steps. The first step estimates the downstream tip-tilt errors as described in this section. The second step numerically shifts the coronagraphic image and realigns the detector and the coronagraph axis as in the reference image I_{cr}. The new image is virtually free of downstream tip-tilt. The third step uses this aligned imaged to estimate the upstream tip-tilt errors and correct for them. In the next section, we present results of this downstream-upstream tip-tilt correction in laboratory conditions.

5. Laboratory performance

We propose to apply the methods described in Sects. 2 and 4 under laboratory conditions. We used the coronagraphic bench, which is described in more detail in Mas et al. (2010). Main components of the bench that we use for this experiment are a diode laser in visible wavelength ($\lambda = 635$ nm), a tip-tilt mirror using piezoelectric actuators, an FQPM coronagraph, a Lyot stop diaphragm, a CCD detector, and a computer that interfaces the detector and the tip-tilt mirror through labview.

5.1. Experimental protocol

The goal of the test is to estimate the tip-tilt errors and correct for them. To introduce large tip-tilt errors (T_x and T_y up to 1.5 λ/D), we willingly varied the laboratory temperature to induce dilatations in the mechanical holders of optical elements.

At the beginning of the experiment, we aligned the source on the coronagraph in order to reach what we considered the best attenuation of the coronagraph (i.e. maximizing A). We recorded the reference image I_{cr} corresponding to this alignment. This reference image corresponds to an initial position of the source and the detector relative to the focal mask. We then raised the temperature of the whole laboratory by a few
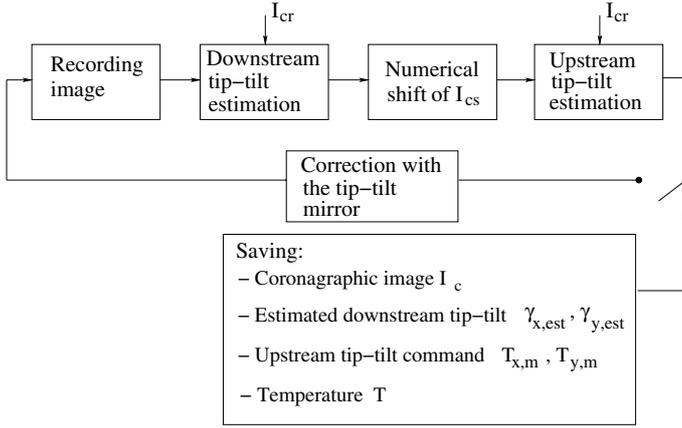
Fig. 9. Block diagram of the experimental protocol. Recording of the data requires opening the control loop.

Fig. 10. Tip-tilt in λ/D applied to the tip-tilt mirror to compensate for the drift upstream of the coronagraph. Values of $T_{x,m}$ in λ/D ($T_{y,m}$) are drawn with triangles (crosses). Experiment 1 (2) data is drawn in blue (black) symbols.

Table 7. Parameters of the experiment.

Wavelength	635 nm
Pupil shape	unobscured disk
Lyot stop size	94%
Pixel size	$\lambda/6.5D$
Image size	$37\lambda/D \times 37\lambda/D$
Quadrant size	$2.6\ \lambda/D$
Inner diameter of the ring Γ	$5.5\ \lambda/D$
Outer diameter of the ring Γ	$9.3\ \lambda/D$
Threshold to select the correlation peak	60%
Number of images averaged in one iteration	100
Closed loop rate	2 Hz
Gain of the closed loop	0.1
Mean total photoelectrons in I_{cr}	7×10^6 e-
Detector readout noise	18 e-

degrees Celsius. Induced thermal dilatations introduced a slow tip-tilt drift, i.e. a movement of the source position compared to the coronagraph axis (upstream tip-tilt) on a minute time scale. At the same time, the detector's centre slowly drifts away from the coronagraph axis (downstream tip-tilt). As soon as the reference image was recorded, we compensated for the downstream shifts and closed the upstream tip-tilt loop.

First, we used the algorithm described in Sect. 4 to estimate the detector shift $\gamma_{x,\,est}$ and $\gamma_{y,\,est}$ compared to the reference image I_{cr}. The numerical shift of the image I_{cs} was done by multiplying by phase ramps in the Fourier domain. From this "recentred" image, we estimated the upstream tip-tilt errors (Eqs. (15) and (16)) and compensated for it applying voltages on the tip-tilt mirror located upstream of the focal mask. We denote $T_{x,m}$ and $T_{y,m}$ thess commands. Reitering this process in closed loop, while the temperature is increasing, we were able to stabilize the beam on the coronagraph controlling the tip-tilt mirror. We can open the loop to save the coronagraphic image, the recorded detector drift (converted in λ/D), the voltages applied on the tip-tilt mirror (converted in λ/D) and the temperature in the laboratory. We recorded the image of the source I_{nc} far from the centre of the coronagraph. The block diagram in Fig. 9 summarizes this control loop.

The parameters of the experiment are given in Table 7. The inner and outer diameters of the ring, threshold of the correlation peak, quadrant size and gain were all defined using test and trial to optimize the stability of the closed loop. The image used to calculate both upstream and downstream tip-tilt errors is the average of 100 images. To reduce the impact of the noise in the experiment, the estimated values of upstream and downstream tip-tilt are multiplied by a 0.1 gain before they are applied to the tip-tilt mirror and the numerical shift software procedure, respectively. The loop frequency is 2 Hz, and we open the loop every minute to record a set of data (images, detector shifts, tip-tilt correction values, and temperatures).

5.2. Experimental results

In this section, we present the results of our two experiments. The first (second) test lasted 30 min and increased the laboratory temperature from 21.2 °C (22.4 °C) to 22.9 °C (24.7 °C). The experimental tip-tilt command $T_{x,m}$ and $T_{y,m}$ applied to the tip-tilt mirror are presented as a function of the temperature variation in Fig. 10. These values are an estimation of the drift between the source and the coronagraph axis during the experiment. The
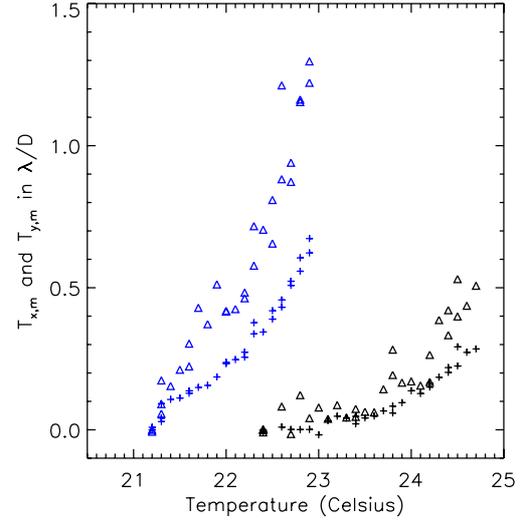
best criterium for measuring the performance of the loop is the attenuation A measured on the recorded images (Eq. (7)). It is plotted versus the temperature in the laboratory (Fig. 11). The attenuation is rather stable compared to the one that could be expected from $T_{x,m}$ and $T_{y,m}$. Indeed, as shown in Sect. 2.2, an additional tip-tilt errors of 0.4 λ/D has a catastrophic impact on an FQPM coronagraph performance (A would drop off to 14).

Even though $T_{x,m}$ and $T_{y,m}$ vary rapidly and are higher than 0.5 λ/D at the end of experiment, the attenuation never drops below 250. We note a dispersion of the attenuation as the temperature increases. This may come from the fact that with increasing temperature, the other aberrations also vary due to beam shift and laboratory turbulence inducing wavefront fluctuations. The median value of the attenuation for both experiments is around 400. This median attenuation can be converted to an upper limit for the median tip-tilt (Eq. (8)) and gives about $6.5 \times 10^{-2}\lambda/D$. The values are reported in Table 8. Compared to the large variation in $T_{x,m}$ and $T_{y,m}$, this clearly indicates that our model is robust enough to be applied in real laboratory conditions. Besides, our control loop behaves well.

The mechanical deformation introduced by thermal effects also creates a slow drift downstream of the coronagraph that creates a shift between the detector and the coronagraph axes
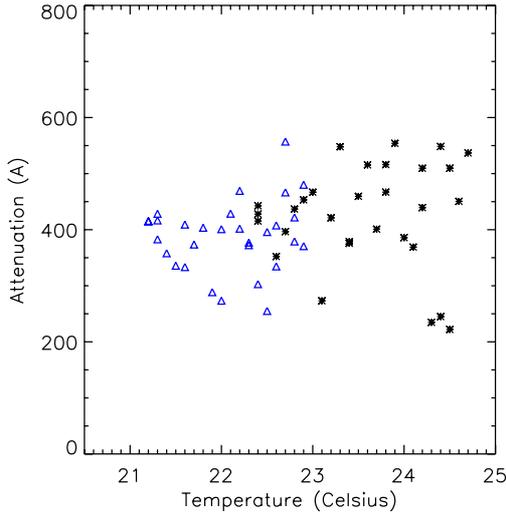
Fig. 11. Stability of the attenuation with respect to the temperature. Experiment 1 (2) data is drawn in blue triangle (black star) symbols.
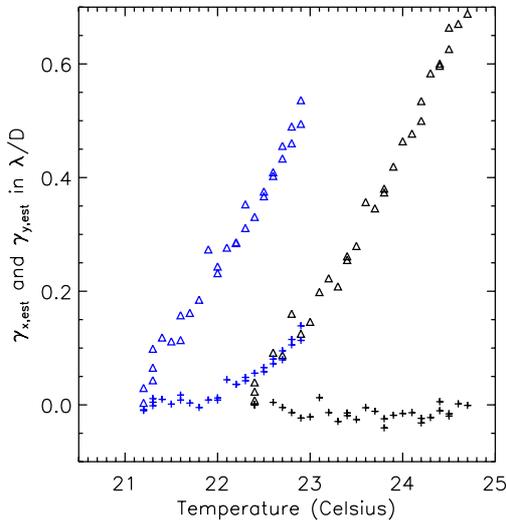

Fig. 12. Position of the detector in λ/D. In y direction: triangles. In x direction: crosses. Same conditions as Fig. 10.

Table 8. Median value of the attenuation A and of the deduced residual tip-tilt errors for two experiments.

Median value	Attenuation (A)	$(T^2_{x,\,\mathrm{est}} + T^2_{y,\,\mathrm{est}})^{1/2}$
Exp 1	400.9	6.7×10^{-2}
Exp 2	439.2	6.4×10^{-2}

(Fig. 12). During the experiments, the detector drifted compared to the coronagraph axis by more than 0.6 λ/D (4 pixels) in the y direction for an increase of 2 °C. If not compensated for in the closed-loop, this large excursion would have completely biased the estimation of the tip-tilt errors, thereby decreasing the attenuation level.

To compare these experimental results with the expected performance simulated in Sect. 3, we need to estimate the WFE level for our experiments. The wavefront metrology of the bench made with a commercial Shack-Hartmann sensor and recorded a few weeks before the experiments were giving WFE between 30 ($\lambda/20$) and 40 nm ($\lambda/16$). We also checked by simulations that the highest attenuation reached (550) is compatible

with these values. We have shown by numerical simulations that for a WFE ϕ rms = 40 nm ($\lambda/20$ for the simulation) and an initial tip-tilt errors between -0.4 and 0.4 λ/D, we were able to reduce the tip-tilt errors down to $2.5 \times 10^{-2}\lambda/D$. On the bench, the control loop decreases a drift variation of the order of 1.5 λ/D to a median error less than $6.5 \times 10^{-2}\lambda/D$. Remember that this value is an upper limit. Indeed, the other high-order aberrations affect the recorded images and may partly or completely set the level of the attenuation. In this case, Eq. (8) used to estimate the tip-tilt errors cannot be directly applied. The developed simulation was essentially focused on studying the best algorithm on images not affected by noise or WFE fluctuations. Adding photon noise, readout noise, flat-field noise, and aberration variations must also change the numerical results. In our simulation, we also studied the measurement of the tip-tilt separately upstream of the coronagraph and of the shift between the coronagraph and the detector. Doing them at the same time certainly slightly decreases the performance of the control loop. More numerical studies are needed to confirm this point.

6. Discussion

Both numerical and laboratory studies use monochromatic light. Since the estimation of upstream tip-tilt errors uses only the central area of I_c, it can certainly be extended to a finite spectral bandwidth. From simulation, we find that Eqs. (9) and (10) are valid for any wavelengths but they change the coefficient β. For a very broad spectral range, limitations may arise from the large dispersion of the diffraction pattern compared to the limited size of the central area S. In this case, achromatic FQPM also need to be used (Mawet et al. 2006; Galicher et al. 2011), but chromatic limitations of the coronagraph must also be taken into account. For the same reason, the impact of coronagraph defects on our tip-tilt estimation needs to be more precisely studied. However, the light that leaks through the coronagraph from these defects adds up to the image as a diffracted spatial structure. It can be partly removed when subtracting I_{cr} but will certainly limit the precision of the estimation in the same way as the high-order WFE errors does. This could explain the lower performance obtained with our experimental bench than with the numerical simulations. We expect the same behaviour, considering central obscuration of the pupil (VLT) or complex pupil geometry (JWST), and this should be verified by numerical simulations. Preliminary simulations also show that our solution can also be applied to other type of phase mask coronagraphs (Dual Zone, vortex coronagraph, Soummer et al. 2003; Mawet et al. 2005). The detailed behaviour of the tip-tilt estimation with these coronagraphs remains to be studied.

The downstream tip-tilt estimation will be only affected by the spectral bandwidth. For a wide spectral range the speckle correlation peak will be enlarged with a lower contrast. Qualitative laboratory tests with both upstream and downstream tip-tilt corrections using a spectral resolution of 16 were also carried out and showed similar behaviour than monochromatic case.

7. Conclusion

In this paper, we have proposed a new method of estimating the tip-tilt errors upstream and downstream of the focal plane mask of a coronagraph by only using the scientific coronagraphic images. The estimation of the upstream errors is based on the computation of intensity differences in x and y directions, splitting

in four quadrants the central part of the coronagraphic image. We used a numerical model to determine the dependence of the intensity differences empirically on the upstream pupil tip and tilt modes for an FQPM coronagraph. In the case of a WFE with no higher terms than tip-tilt, we found the laws that drives the coupling between the intensity differences in x and y directions. We thus derived the estimators of tip-tit errors. Higher order terms induce slightly asymmetric speckle pattern in focal plane, and the tip and tilt estimation is affected by such an error. Nevertheless, we demonstrated by numerical simulations that using this law, even with the presence of high-order WFE, we are able to estimate and to compensate for in a few iterations tip and tilt upstream of the coronagraph with a $1.3 \times 10^{-2} \lambda/D$ accuracy for 20 nm rms WFE ($\lambda/40$) and $2.5 \times 10^{-2} \lambda/D$ for 40 nm rms ($\lambda/20$). Such a performance is required for the planet imager systems under development as SPHERE, and MIRI/JWST. Our method should be directly applicable to them. The attenuation brought by the coronagraph can be improved most often by the tip-tilt compensation when compared to the initial reference image corresponding to the best alignment.

We also show that the tip-tilt errors downstream of the focal plane mask can bias the upstream tip-tilt error estimation, because they induce a shift of the detector array with respect to the coronagraph axis. We then proposed to estimate the downstream errors measuring the correlation of the speckles in a ring around the centre of the coronagraphic images. We demonstrated from our numerical simulations that we can estimate the detector position with $10^{-2} \lambda/D$ accuracy.

We applied the two methods on our laboratory bench to control the tip-tilt errors upstream and downstream of the focal plane mask at the same time, using the coronagraphic image with no additional channel. We succeeded in stabilizing the beam on the focal plan mask with accuracy much better than $6.5 \times 10^{-2} \lambda/D$. The performance is mostly limited by high-orders of the WFE.

This tip-tilt control technique is now operational on our high-contrast optical imaging bench (Mas et al. 2010), and it will be running in parallel with the speckle suppression technique called self-coherent camera (Galicher et al. 2008).

Appendix A

All variables used in this paper are defined in Table A.1.

Appendix B

We develop the formalism and explain the method to derive estimators $T_{x,\text{est}}$ and $T_{y,\text{est}}$. We start by recalling the expression of ΔI_x and ΔI_y:

$$\frac{\Delta I_x}{\beta} = T_x^3 + \alpha T_x T_y^2, \tag{B.17}$$

$$\frac{\Delta I_y}{\beta} = T_y^3 + \alpha T_y T_x^2, \tag{B.18}$$

where T_x and T_y are the tip-tilt errors. α and β are coefficients determined by numerical simulations by analysing the behaviour of ΔI_x and ΔI_y in the function of T_x and T_y. The rigorous justification of this relation is postponed to a forthcoming paper. To determine α, we consider the case with $\phi = 0$ and $T_x \gg T_y$: $T_{x_1} = 0.4\lambda/D$ and $T_{y_1} = 10^{-6}\lambda/D$, for instance. We can derive α from the corresponding measured values of ΔI_{x_1} and ΔI_{y_1} by

$$\alpha = \frac{T_{x_1}}{T_{y_1}} \frac{\Delta I_{y_1}}{\Delta I_{x_1}}. \tag{B.19}$$

Table A.1. List of the variables used in this paper.

	Variables
A	Coronagraphic attenuation peak
C	Image correlation between I_{cs} and I_{cr}
D	Telescope diametre
I_{c}	Intensity of the coronagraphic image
I_{cr}	Intensity of the coronagraphic reference image corresponding to the best attenuation
I_{cs}	Intensity of the shifted coronagraphic image
I_i	Normalized integrated intensity in each quadrant Q_i
I_{nc}	Intensity of the non coronagraphic image
L	Lyot stop
M	Focal mask
Q_i	Quadrants in the central area S of the coronagraphic image
R	Ratio $\frac{T_x}{T_y}$
S	Central area of the coronagraphic image
T_x (T_y)	x-tilt (y-tilt) upstream of the coronagraph
$T_{x,m}$ and $T_{y,m}$	Command applied on the tip-tilt mirror
α, β	Multiplicative coefficients defined by numerical simulation
Γ	Ring-shape mask
γ_x (γ_y)	Shift of the detector in x (y) direction
$\gamma_{x,\text{est}}$ ($\gamma_{y,\text{est}}$)	Estimated shift of the detector in x (y) direction
ΔI_x (ΔI_y)	Intensity difference in x (y) direction in the central area S
$\Delta I_{x,r}$ ($\Delta I_{y,r}$)	Intensity difference in x (y) direction in the central area of the coronagraphic reference image ($\phi \neq 0$)
Δ_x (Δ_y)	Eqs. (11) and (12)
λ	wavelength
ϕ	Wavefront error (WFE)
ψ'	Monochromatic electric field upstream of the coronagraph
ψ	Monochromatic electric field downstream of the coronagraph
ξ, ν	Spatial coordinates in the entrance pupil

For an FQPM, we find $\alpha = 4$. To determine β, we set $\phi = 0$ and $T_y = 0$, we scan different values for T_{x_2} from $-\lambda/D$ to λ/D (here, 40 values). Since there is no WFE, hence no additional y-tilt, $\frac{\Delta I_{x_2}}{\beta} = T_{x_2}^3$ and $\frac{\Delta I_{y_2}}{\beta} = 0$ (Eqs. (B.17) and (B.18)). For each T_{x_2}, we measure ΔI_{x_2}. As a result, we get β as the slope of ΔI_{x_2} versus T_{x_2}. For $T_x > 0.4\lambda/D$, the PSF is badly coronagraphied. In a realistic case, we avoid such a relatively large tip. We then find $\beta = 0.59$ corresponding to $T_x < 0.4\lambda/D$.

To estimate the tip tilt errors from the measurements, we first have to inverse Eqs. (11) and (12). If T_y is not nought, we derive this expression with respect to $R = T_x/T_y$

$$\Delta_x = \left(R^3 + 4R\right) T_y^3, \tag{B.20}$$

$$\Delta_y = \left(1 + 4R^2\right) T_y^3. \tag{B.21}$$

It can also be written as

$$R^3 - 4R^2 \frac{\Delta_x}{\Delta_y} + 4R - \frac{\Delta_x}{\Delta_y} = 0, \tag{B.22}$$

where R is determined as the solution of this equation. We then derive the general expressions of $T_{x,\text{est}}$ and $T_{y,\text{est}}$:

$$T_{x,\text{est}} = \left(R^2 \frac{\Delta_x}{(R^2+4)}\right)^{1/3} \tag{B.23}$$

$$T_{y,\text{est}} = \left(\frac{\Delta_y}{(1+4R^2)}\right)^{1/3}. \tag{B.24}$$

The estimators depend on the value of R.

We represent the plot of Eq. (B.22) by the dotted line in Fig. B.1 for $\phi = 0$. This equation most often has a unique pure real solution R for a given ratio Δ_x/Δ_y, which is

$$R = -\frac{U}{3.2^{1/3}} + \frac{2^{1/3}\left(12 - 16\left(\frac{\Delta_x}{\Delta_y}\right)^2\right)}{3U} + \frac{4\left(\frac{\Delta_x}{\Delta_y}\right)}{3}, \tag{B.25}$$

with

$$U = \left(-128\left(\frac{\Delta_x}{\Delta_y}\right)^3 + 3\sqrt{3}\right.$$
$$\times \sqrt{256\left(\frac{\Delta_x}{\Delta_y}\right)^4 - 517\left(\frac{\Delta_x}{\Delta_y}\right)^2 + 256}$$
$$\left. + 117\left(\frac{\Delta_x}{\Delta_y}\right)\right)^{1/3} \tag{B.26}$$

$$U = \left(-128\left(\frac{\Delta_x}{\Delta_y}\right)^3 + 3\sqrt{3}\right.$$
$$\sqrt{256\left(\frac{\Delta_x}{\Delta_y}\right)^4 - 517\left(\frac{\Delta_x}{\Delta_y}\right)^2 + 256}$$
$$\left. + 117\left(\frac{\Delta_x}{\Delta_y}\right)\right)^{1/3}. \tag{B.27}$$

From Fig. B.1, we also see that, for $\frac{\Delta_x}{\Delta_y}$ around 1 or -1, the ratio R can have two or three solution values.

We manage the different cases as

– For $0.8 < |\frac{\Delta_x}{\Delta_y}| < 1.1$, R can take two or three real values, all close to 1. In this case, we approximate the ratio R by taking $R = 1$. Then we deduce that the tip and tilt estimations are

$$T_{x,\text{est}} = \left(\frac{\Delta_x}{5}\right)^{1/3}, \tag{B.28}$$

$$T_{y,\text{est}} = \left(\frac{\Delta_y}{5}\right)^{1/3}. \tag{B.29}$$

– For $|\frac{\Delta_x}{\Delta_y}| > 1.1$ and $|\frac{\Delta_x}{\Delta_y}| < 0.8$, we have a unique pure real solution

$$T_{x,\text{est}} = \left(\frac{R^2\Delta_x}{(R^2+4)}\right)^{1/3}, \tag{B.30}$$

$$T_{y,\text{est}} = \left(\frac{\Delta_y}{(1+4R^2)}\right)^{1/3}. \tag{B.31}$$
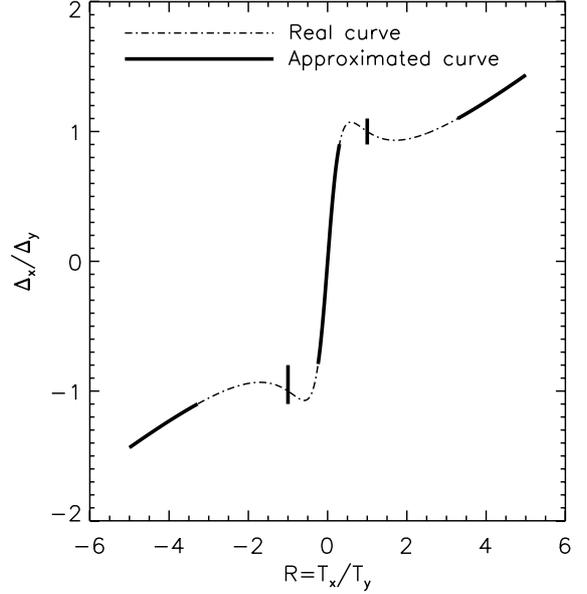

Fig. B.1. Dotted line Δ_x/Δ_y versus $R = T_x/T_y$ as in Eq. (B.22). Continuous curves: approximated behaviour. $\phi = 0$ nm rms.

– For $\Delta_y = 0$, the same expressions are valid replacing Δ_x by Δ_y (and inversely), R by $1/R$ and $T_{x,\text{est}}$ by $T_{y,\text{est}}$ (and inversely).
– In the case where Δ_x and Δ_y are both nought, $T_{x,\text{est}}$ and $T_{y,\text{est}}$ are also nought.

References

Abe, L., Dominiciano de Sousa, A., Jr., Vakili, F., & Gay, J. 2003, A&A, 400, 385
Beuzit, J.-L., Feldt, M., Dohlen, K., et al. 2008, SPIE Proc., 7014
Boccaletti, A., Baudoz, P., Baudrand, J., Reess, J. M., & Rouan, D. 2005, AdSpR, 36, 1099
Galicher, R., Baudoz, P., & Rousset, G. 2008, A&A, 488, L9
Galicher, R., Baudoz, P., & Baudrand, J. 2011, A&A, 530, A43
Guyon, O., Pluzhnik, E. A., Kuchner, M. J., Collins, B., & Ridgway, S. T. 2006, ApJ, 167, 81
Guyon, O., Matsuo, T., & Angel, R. 2009, ApJ, 693, 75
Lloyd, J. P., & Sivaramakrishnan, A. 2005, ApJ, 621, 1153
Lloyd, J. P., Gavel, D. T., Graham, J. R., et al. 2003, SPIE Proc., 4860, 171
Macintosh, B. A., Graham, J. R., Palmer, D. W., et al. 2008, SPIE Proc., 7015
Marois, C., Lafrenière, D., Macintosh, B., & Doyon, R. 2006, ApJ, 647, 612
Mas, M., Baudoz, P., Rousset, G., Galicher, R., & Baudrand, J. 2010, SPIE Proc., 7735
Mawet, D., Riaud, P., Absil, O., & Surdej, J. 2005, ApJ, 633, 1191
Mawet, D., Riaud, P., Baudrand, J., et al. 2006, A&A, 448, 801
Perrin M. D., Sivaramakrishnan, A., Makidon, R. B., Oppenheimer, B. R., & Graham, J. R. 2003, ApJ, 596, 702
Rouan, D., Riaud, P., Boccaletti, A., Clénet, Y., & Labeyrie, A. 2000, PASP, 112, 1479
Rouan, D., Riaud, P., & Baudrand, J. 2002, European Southern Observatory Conference and Workshop Proc., 58, 193
Shaklan, S. B., & Green, J. J. 2005, ApJ, 628, 474
Sivaramakrishnan, A., & Oppenheimer, B. R. 2006, ApJ, 647, 620
Sivaramakrishnan, A., Soummer, R., Sivaramakrishan, A. V., et al., 2005, ApJ, 634, 1416
Sivaramakrishnan, A., Soummer, R., Pueyo, L., Wallace, J. K., & Shao, M. 2008, ApJ, 688, 701
Soummer, R., Dohlen, K., & Aime, C. 2003, ESA Spec. Publ., 539, 599
Tyler, G. L., & Fried, D. L. 1982, JOSA, 72, 804
Zimmerman, N., Oppenheimer, B. N., Hinkley, S., et al. 2010, ApJ, 709, 733